Journal of Clinical and Translational Hepatology **2025**
DOI: 10.14218/JCTH.2025.00416

Original Article

IL1RA$^+$ Myeloid-derived Suppressor Cells Activate Epithelial-mesenchymal Transition to Facilitate Lymphatic and Hepatic Metastasis in Pancreatic Ductal Carcinoma

Huan Liu[1], Jian Zhang[1], Shengnan Lv[1], Xinyu Peng[1], Han Liu[1], Haijun Li[2*] and Feng Wei[1*]

[1]Department of Hepatobiliary and Pancreatic Surgery, General Surgery Center, The First Hospital of Jilin University, Changchun, Jilin, China; [2]Institute of Translational Medicine, The First Hospital of Jilin University, Changchun, Jilin, China

Received: August 21, 2025 | **Revised:** August 28, 2025 | **Accepted:** September 05, 2025 | **Published online:** September 24, 2025

Abstract

Background and Aims: Hepatic metastasis (HM) and lymph node metastasis in pancreatic ductal adenocarcinoma (PDAC) are associated with worse overall survival, largely due to the immunosuppressive microenvironment. However, the key immunosuppressive cells within this microenvironment remain inadequately defined. This study aimed to identify the cells contributing to HM and lymph node metastasis in PDAC and to investigate their regulatory mechanisms. ***Methods:*** Single-cell RNA sequencing was used to profile the tumor microenvironment in HM, lymph node-negative, and lymph node-positive (LNP) PDAC tissues. Bioinformatic analyses revealed subtypes of immunosuppressive myeloid-derived suppressor cells (MDSCs). Immunofluorescence and flow cytometry were performed to detect the distribution and proportion of interleukin-1 receptor antagonist (IL1RA$^+$) MDSCs. The immunosuppressive and pro-tumorigenic functions of IL1RA$^+$ MDSCs were analyzed using enzyme-linked immunosorbent assay, quantitative reverse transcription polymerase chain reaction, Western blotting, and Transwell assays. Patient-derived xenograft mouse models were employed to validate the role of IL1RA$^+$ MDSCs *in vivo*. ***Results:*** Polymorphonuclear-MDSCs were found to be recruited to metastatic PDAC tissues. Among these, IL1RA$^+$ MDSCs were enriched in HM/LNP tissues and correlated with poorer prognosis. IL1RA$^+$ MDSCs promoted M2 macrophage polarization and suppressed the activity of natural killer cells and cytotoxic T cells. Furthermore, IL1RA$^+$ MDSCs accelerated PDAC migration and progression by upregulating epithelial–mesenchymal transition-related proteins in both *in vitro* and *in vivo* models. ***Conclusions:*** IL1RA$^+$ MDSCs represent a key immunosuppressive and pro-tumorigenic subtype in HM/LNP PDAC, providing a solid theoretical basis for prognostic prediction and the development of immunotherapeutic strategies targeting these cells in HM/LNP PDAC.

Citation of this article: Liu H, Zhang J, Lv S, Peng X, Liu H, Li H, *et al*. IL1RA$^+$ Myeloid-derived Suppressor Cells Activate Epithelial-mesenchymal Transition to Facilitate Lymphatic and Hepatic Metastasis in Pancreatic Ductal Carcinoma. J Clin Transl Hepatol 2025. doi: 10.14218/JCTH.2025.00416.

Introduction

Pancreatic ductal adenocarcinoma (PDAC) is one of the most lethal malignancies, with a five-year overall survival rate of only 13%, largely attributable to its propensity for early metastasis.[1] Approximately 57% of PDAC patients present with metastatic disease at diagnosis.[2] Among them, hepatic metastasis (HM) and lymph node metastasis (LNM) occur frequently and predict poorer prognosis.[3,4] Although the poor prognosis of PDAC has often been attributed to HM and LNM, which contribute to extensive dissemination into peripheral tissues and distant metastasis,[5] other potential mechanisms remain unexplored. Therefore, investigating the underlying mechanisms of HM and LNM in PDAC and identifying strategies to inhibit them may highlight novel therapeutic approaches and ultimately improve the five-year overall survival rate.

The occurrence of HM and LNM is associated with an immunosuppressive tumor microenvironment (TME) and activation of epithelial-mesenchymal transition (EMT) in tumor cells.[6] PDAC is characterized by its immunosuppressive TME, which is strongly associated with HM and LNM.[7,8] Multiple immune cells, including myeloid-derived suppressor cells (MDSCs), M2 macrophages, dendritic cells, regulatory T cells, and group 3 innate lymphoid cells, have been identified as contributors to the immunosuppressive TME that promotes HM and LNM in PDAC.[9–11] MDSCs are a heterogeneous population of myeloid cells that strongly inhibit the anticancer functions of effector immune cells.[12] Recent studies have revealed distinct immunosuppressive functions of various MDSC subtypes in remodeling the TME. For instance, polymorphonuclear MDSCs (PMN-MDSCs) suppress tumor-specific immune responses by regulating the endoplasmic reticulum stress response in mice with lung cancer and lymphoma,[13] while monocytic MDSCs (M-MDSCs) upregulate secreted phosphoprotein 1 to compensate for CD274 function,

---

Keywords: Pancreatic cancer; Interleukin-1 receptor antagonist; IL1RA; Myeloid-derived suppressor cells; Lymphatic metastasis; Hepatic metastasis.

[*]**Correspondence to:** Feng Wei, Department of Hepatobiliary and Pancreatic Surgery, General Surgery Center, The First Hospital of Jilin University, Changchun, Jilin 130021, China. ORCID: https://orcid.org/0000-0001-8451-4516. Tel/Fax: +86-431-81875161, E-mail: wei_feng@jlu.edu.cn; Haijun Li, Institute of Translational Medicine, The First Hospital of Jilin University, Changchun, Jilin 130021, China. ORCID: https://orcid.org/0000-0002-2515-3076. Tel/Fax: +86-431-88783044, E-mail: hjli2012@jlu.edu.cn.

thereby promoting immune escape in PDAC.[14] Despite growing insights into the functions of MDSCs in various cancer types, their relationship with HM and LNM in PDAC remains poorly explored.

The interleukin (IL)-1 subfamily consists of IL-1α, IL-1β, IL-33, and IL-1 receptor antagonist (IL1RA).[15] Within this subfamily, IL1RA, encoded by *IL1RN*, serves as a competitive inhibitor of IL-1 ligands, counteracting IL-1 signaling to modulate immune responses.[16] In the context of its immunosuppressive role in the TME, IL1RA has been shown to interact with the cholinergic muscarinic 4 receptor, promoting an M2-like phenotype in monocytes and enhancing tumor aggressiveness in prostate cancer.[17] Beyond immune regulation, IL1RA can also reverse the suppressive effects of methionine deprivation, thereby promoting glioma cell proliferation.[18] Although emerging evidence suggests that IL1RA contributes to tumor progression, the specific roles of IL1RA$^+$ MDSCs in HM and LNM of PDAC remain poorly defined.

EMT is a process through which epithelial cells lose their characteristic features and acquire mesenchymal traits, enabling tumor cells to invade adjacent tissues, including lymph nodes.[19] EMT-related proteins such as Snail, N-cadherin, and E-cadherin have been correlated with HM in PDAC[20] and with LNM in oral squamous cell carcinoma and cervical cancer.[21,22] The EMT pathway is widely recognized as being activated early during metastasis or in response to oxidative stress.[23] Importantly, immune cells such as macrophages have been shown to drive EMT through the secretion of cytokines like IL-1β and transforming growth factor (TGF)-β in breast and lung cancers.[24,25] However, whether EMT can be driven by MDSCs remains unclear.

To identify immune-cell subsets that drive HM and LNM in PDAC, we performed single-cell RNA sequencing (scRNA-seq) and discovered a novel subtype of IL1RA$^+$ MDSCs aberrantly enriched in HM and lymph node-positive (LNP) PDAC. IL1RA$^+$ MDSCs exert potent immunosuppressive effects on macrophages, NK cells, and T cells by inhibiting the IL-1 pathway. Moreover, IL1RA$^+$ MDSCs promote PDAC cell migration by activating the EMT pathway in a VEGFA-dependent manner. Treatment with axitinib, a VEGFA-targeted drug, effectively abolished the influence of IL1RA$^+$ MDSCs on PDAC cells. These findings reveal a novel mechanism whereby IL1RA$^+$ MDSCs promote HM and LNM by activating EMT and remodeling the immunosuppressive microenvironment, suggesting that targeting IL1RA$^+$ MDSCs may represent a promising therapeutic strategy in PDAC.

Methods

Patient information and sample acquisition

Fresh tissue specimens were collected from a cohort of 24 PDAC patients at the First Affiliated Hospital of Jilin University (Changchun, China) between 2023 and 2024. For resectable primary pancreatic cancer, all patients had non-metastatic PDAC, had not received prior preoperative treatment, and were confirmed by pathological assessment. Patients with other malignancies, comorbidities, or those who had received neoadjuvant therapy were excluded from the study. Six patients underwent scRNA-seq; three of them were pathologically diagnosed with LNM. In addition, one hepatic metastasis sample was collected for scRNA-seq. One PDAC tumor tissue specimen was obtained from a 63-year-old woman who underwent radical resection for the establishment of patient-derived xenograft (PDX) models. Tissue slides from another cohort of 10 PDAC patients were obtained from the Department of Pathology for multiplex immunofluorescence assays. Blood samples from three healthy donors were collected for *in vitro* immune functional assays. All participants were informed about the use of their samples for experimental studies and PDX model establishment. This study was approved by the Ethics Committee of the First Affiliated Hospital of Jilin University (Approval No. 2019180) and conducted in accordance with recognized ethical guidelines.

Tissue dissociation and single-cell suspension preparation

For scRNA-seq, PDAC and HM tissues were preserved in GEXSCOPE Tissue Preservation Solution (Singleron Biotechnologies, Nanjing, China) immediately after surgery and transported to the Singleron laboratory on ice packs within 48 h. The specimens were washed with Hank's balanced salt solution (HBSS; Gibco, Grand Island, NY, USA) and cut into 1–2 mm pieces. Tissue fragments were digested with GEXSCOPE Tissue Dissociation Solution (Singleron Biotechnologies) at 37°C for 15 m with continuous agitation. Once cell counts exceeded 20,000, the resulting suspension was filtered through 40-μm sterile strainers (Falcon, Marlboro, NY, USA) and centrifuged at 300 × g for 5 m (Eppendorf, Hamburg, Germany). Pellets were resuspended in 1 mL phosphate-buffered saline (PBS; Hyclone, Logan, UT, USA), and RBC lysis buffer (Rochester, MI, USA) was added to remove red blood cells. The mixture was centrifuged at 500 × g for 5 m at 15–25°C and resuspended in PBS (Hyclone). The final cell concentration was adjusted to 1×10^5 cells/mL, and downstream processing proceeded once cell viability exceeded 80%.

scRNA-seq

scRNA-seq was performed as previously described.[26] Single-cell suspensions at 1×10^5 cells/mL were loaded onto microfluidic devices, and scRNA-seq libraries were prepared using the GEXSCOPE Single-Cell RNA Library Kit (Singleron Biotechnologies), following the manufacturer's protocol. Libraries were diluted to 4 nM, pooled, and sequenced on an Illumina HiSeq X platform with 150 bp paired-end reads. Raw reads were processed using fastQC and fastp to remove low-quality reads, while poly-A tails and adaptor sequences were trimmed using cutadapt. After quality control, reads were aligned to the GRCh38 reference genome (Ensembl version 92 annotation) using STAR. Gene and UMI counts were generated using featureCounts, and expression matrices were constructed for downstream analyses.

scRNA-seq data integration and quality control

The scRNA-seq data from the study cohort ($n = 7$) were integrated with five publicly available datasets: CRA001600, GSE197177, GSE229413, GSE242230/syn5241395, and OEP003254. Cells with <200 or >5,000 detected genes, or with >10% mitochondrial reads, were excluded. The Seurat package was used for normalization and scaling of the expression matrix. Principal component analysis was performed on the top 2000 highly variable genes for dimensionality reduction. To correct for batch effects across samples and datasets, the Harmony package was applied.

Unsupervised clustering, marker identification, and cell type annotation

Unsupervised clustering was performed using a graph-based approach with the top 30 principal components and a resolution of 0.8. Clusters were visualized using Uniform Manifold Approximation and Projection (UMAP) and t-distributed Stochastic Neighbor Embedding (tSNE). Clusters were annotated based on canonical marker expression to identify cell types. For myeloid cell subsets, the 'FindAllMarkers' function in Seurat was used to identify the top five most highly expressed genes per subset. Myeloid cells with low HLA-DR expression were defined as MDSCs.[27]

Pathway analysis and single-cell trajectories of neutrophil-derived MDSCs

Differentially expressed genes (DEGs) in neutrophil-derived MDSCs were identified using the 'FindAllMarkers' function in Seurat (min.pct = 0.25, logfc.threshold = 0.25). Gene Ontology enrichment analysis was performed with the clusterProfiler R package. Pseudotime analysis of neutrophil-derived MDSC developmental trajectories was conducted using the Monocle2 R package with default parameters, as recommended.

Cell-cell interaction analysis

Cell-cell interactions among TME cell types were predicted using CellPhoneDB based on the normalized expression matrix generated by Seurat.

Multiplex immunofluorescence staining

Formalin-fixed, paraffin-embedded tumor slides from 10 PDAC patients (five lymph node-negative (LNN) and five LNP) were obtained from the Department of Pathology at the First Hospital of Jilin University. Primary antibodies included CD11b (Abcam, Cambridge, UK), CD68 (Proteintech, Wuhan, China), MPO (Abcam), IL1RA (Proteintech), and VEGFA (Proteintech). Antibody concentrations are listed in Supplementary Table 1. Secondary horseradish peroxidase-conjugated antibodies were applied, and nuclei were counterstained with DAPI (4′,6-diamidino-2-phenylindole). Slides were imaged using a Nikon DS-U3 microscope (Nikon, Tokyo, Japan; 10× magnification).

Cell culture

Human PDAC cell lines PANC-1 and AsPC-1 were purchased from Fenghui Biotechnology Co., Ltd. (Changsha, China) for Transwell and Western blotting assays. THP-1 and K562 cells were obtained from the Cell Bank of Shanghai Institutes for Biological Sciences, Chinese Academy of Sciences (Shanghai, China). AsPC-1 and K562 were cultured in Roswell Park Memorial Institute (hereinafter referred to as RPMI)-1640 medium (Corning, NY, USA), while PANC-1 was cultured in Dulbecco's modified Eagle's medium (Corning) at 37°C in a humidified incubator with 5% CO_2. All media were supplemented with 10% fetal bovine serum (Gibco) and 1% penicillin/streptomycin (100 µg/mL; Gibco). All cell lines were authenticated by short tandem repeat profiling and confirmed to be mycoplasma-free using the MycoAlert™ Mycoplasma Detection Kit (Lonza, Basel, Switzerland). None of the cell lines used is listed in the database of commonly misidentified cell lines maintained by the International Cell Line Authentication Committee (ICLAC).

Flow cytometry analysis of PDAC tissues

Tumor-infiltrating immune cells were isolated from PDAC tissues by mincing tumors into 1–2 mm fragments, followed by enzymatic digestion with 200 U/mL collagenase type IV (Gibco) and 200 µg/mL DNase I (Solarbio, Beijing, China) at 37°C with agitation in a water bath for 2 h. Dissociated cells were filtered through a 70-µm strainer (Merck Millipore, Burlington, MA, USA) and centrifuged at 300 × g for 7 m. Cells were washed, resuspended at 1 × 10^6 cells/50 µL in FACS buffer, and stained with antibody panels for 30 min at 4°C.

Panel 1: anti-HLA-DR FITC (BioLegend, CA, USA), anti-CD11b PE (BioLegend), anti-CD33 APC (BioLegend), anti-CD14 V450 (BD Biosciences, CA, USA), anti-CD66b PE-Cy7 (BioLegend), and anti-CD45 APC/Cy7 (BioLegend).

Panel 2: anti-HLA-DR BV421 (BioLegend), anti-CD11b PE (BioLegend), anti-CD33 APC (BioLegend), anti-CD14 PerCP (BioLegend), anti-CD66b PE-Cy7 (BioLegend), and anti-CD45 APC/Cy7 (BioLegend).

For intracellular staining, anti-IL1RA FITC (eBioscience™, San Diego, CA, USA) was used. Cells were fixed and permeabilized using the BD Cytofix/Cytoperm™ Fixation/Permeabilization Kit (BD Biosciences, San Diego, CA, USA) following the manufacturer's instructions.

Samples were analyzed using a BD Fortessa flow cytometer (BD Biosciences). For Panel 1, 7-AAD (BioLegend) was added to exclude dead cells. Data were analyzed with FlowJo software (Version 10.8.1; TreeStar, Ashland, OR, USA). Detailed antibody information is presented in Supplementary Table 2.

Cell isolation and flow cytometry sorting

Peripheral blood samples were collected from three healthy donors at the First Hospital of Jilin University. Peripheral blood mononuclear cells (PBMCs) were isolated using Ficoll density gradient centrifugation (Lymphoprep; Stemcell, BC, Canada). PBMCs were washed, resuspended at 1 × 10^8 cells/50 µL in FACS buffer, and stained with anti-CD3 PerCP (BioLegend) and anti-CD56 FITC (BioLegend) for 30 m at 4°C. $CD3^+$ T cells and $CD3^-CD56^+$ NK cells were sorted using a BD Influx flow cytometer (BD Biosciences) for subsequent *in vitro* immune assays.

For tumor-infiltrating immune cells, isolated cells were stained with anti-HLA-DR BV421 (BioLegend), anti-CD11b PE (BioLegend), anti-CD66b PE-Cy7 (BioLegend), anti-GPR109 AF647 (BioLegend), and anti-CD182 FITC (BioLegend).

$HLA\text{-}DR^{-/dim}CD11b^+CD66b^+GPR109^+CD182^{-/dim}$ MDSCs were isolated using a BD Influx flow cytometer (BD Biosciences). Dead cells were removed prior to sorting using the Dead Cell Removal Kit (Miltenyi Biotec, Bergisch Gladbach, Germany) according to the manufacturer's protocol. To prepare conditioned medium (CM), $GPR109^+CD182^{-/dim}$ MDSCs were cultured for 48 h. The supernatant was filtered through a 0.22-µm membrane filter (Merck Millipore) and centrifuged at 1,000 × g for 10 m at 4°C.

RNA isolation and quantitative reverse transcription polymerase chain reaction (qRT-PCR)

Total RNA was extracted from NK cells, T cells, and THP-1 cell pellets using TRIzol reagent (Invitrogen, CA, USA). RNA was reverse-transcribed into complementary DNA using a kit from Takara (Tokyo, Japan). qRT-PCR was performed with TB Green Premix Ex Taq™ (Takara). Relative expression levels were calculated using the $2^{-\Delta\Delta Ct}$ method. Primer sequences are listed in Supplementary Table 3.

Western blotting

PANC-1 cells were cultured in CM derived from IL1RA⁺ MDSCs for 48 h. Cells were lysed with RIPA buffer (Merck Millipore), and protein concentration was quantified using a BSA protein assay kit. Equal amounts of protein were separated by sodium dodecyl sulfate-polyamide gel electrophoresis and transferred to polyvinylidene fluoride membranes (Merck Millipore). Membranes were blocked with 5% skim milk and incubated overnight at 4°C with primary antibodies. After washing three times with TBST (10 m each), membranes were incubated with secondary antibodies for 45 m at room temperature. Immunoreactive bands were visualized using a Tanon imaging system. Antibody details and dilutions are listed in Supplementary Table 1.

Enzyme-linked immunosorbent assay (ELISA)

NK cells, T cells, and THP-1 cells (1×10^5 each) were cultured in CM derived from IL1RA$^+$ MDSCs for 48 h. Supernatants were collected and analyzed for cytokine production using ELISA kits according to the manufacturers' protocols. The ELISA kits included assays for MCP-4/CCL13 (Invitrogen), TNF-α (Invitrogen), TGF-β1 (Invitrogen), IL-1β (Invitrogen), IL-2 (Invitrogen), IL-10 (Invitrogen), IFN-γ (Invitrogen), and Granzyme B (GZB; Invitrogen). Detailed kit information is provided in Supplementary Table 4.

Lactate dehydrogenase (LDH) release assay

Freshly isolated NK cells (1×10^5) from PBMCs were cultured in IL-2-supplemented RPMI-1640 medium. IL1RA$^+$ MDSCs were sorted from PDAC tissue samples using flow cytometry. Target cells (K562 leukemia cells) were prepared at a concentration of 1×10^5 cells/mL. NK cells, K562 cells, and MDSCs were co-cultured in 96-well U-bottom plates at an effector-to-target-to-MDSC (E:T:M) ratio of 10:1:1 (1×10^5 NK cells, 1×10^4 K562 cells, and 1×10^4 MDSCs per well). After 6 h of incubation, 150 µL of supernatant was collected from each well after centrifugation ($200 \times g$, 10 m), mixed with 50 µL of LDH reaction mix (Beyotime, Shanghai, China), incubated for 20–30 m in the dark, and measured at OD$_{490}$. NK-specific cytotoxicity was calculated as:

$$\%\ \text{Cytotoxicity} = \frac{\text{Maximum OD} - \text{Spontaneous OD}}{\text{Experimental OD} - \text{Spontaneous OD}} \times 00\%.$$

Transwell assay

A total of 200 µL of serum-free medium containing 1×10^5 PANC-1 or AsPC-1 cells was added to the upper chamber of a Transwell plate (Corning). IL1RA$^+$ MDSCs were pretreated with or without 5 nM axitinib for 48 h. Then, 600 µL of complete medium containing 10% fetal bovine serum (Gibco) was added to the lower chamber. After 24 h, cells in the upper chamber were fixed with 4% paraformaldehyde and stained with 1× DAPI. Cells remaining on the upper surface of the membrane were removed with cotton swabs. Images were captured using an Olympus IX73 microscope system (Olympus, Tokyo, Japan).

Patient-derived xenograft (PDX) models

PDAC tumor tissue was obtained from a 63-year-old female patient who underwent radical resection at the First Hospital of Jilin University to establish PDX models. Fresh PDAC tissue was cut into 3–5 mm^3 pieces and implanted into the right flanks of six-week-old female BALB/c nude mice (F1 generation). Tumor volumes were measured twice weekly. When tumors reached 1,000 mm^3, mice were sacrificed, xenografts harvested, and implanted into a second generation of mice (F2 generation). Once F2 tumors reached 1,000 mm^3, xenografts were surgically removed and segmented for further animal experiments.

Xenograft models

Nine five-week-old BALB/c nude mice were purchased from SiPeiFu Biotechnology (Beijing, China) and housed in a positive-pressure barrier facility with HEPA-filtered air. The nine mice were randomly divided into three groups: negative control, IL1RA$^+$ MDSCs, and IL1RA$^+$ MDSCs + axitinib. Tumor tissue was cut into 1 mm^3 blocks and implanted subcutaneously into the right flank of six-week-old female BALB/c nude mice. When tumors reached 3 mm in diameter, 5×10^4 IL1RA$^+$ MDSCs were subcutaneously injected into three mice from the IL1RA$^+$ MDSC group. Axitinib (Selleck Chemicals, Houston, TX, USA) was dissolved in 0.5% carboxymethylcellulose/H$_2$O·HCl (g/v, pH 2–3) and administered orally at 30 mg/kg twice daily to the treatment group, as previously described.[27] Tumor volumes were measured twice a day. Mice were sacrificed by cervical dislocation after six weeks, and tumor weights and volumes were recorded post-resection. All animal studies complied with the Institutional Animal Care and Use Committee of Changchun Veterinary Research Institute (Approval No. 2024-11-066).

Statistical analysis

Statistical analyses were performed using GraphPad Prism 8.0 software (GraphPad Software Inc., La Jolla, CA, USA). Kaplan–Meier survival curves and log-rank tests were used to compare overall survival between LNN and LNP PDAC patients. Data are presented as the mean ± standard deviation. Results represent at least three independent experiments. Statistical differences between two groups were determined using an unpaired, two-tailed Student's t-test. Comparisons among multiple groups were made using one-way analysis of variance. The Chi-square test was applied to assess differences between categorical variables. A p-value < 0.05 was considered statistically significant and indicated as follows: $*p < 0.05$, $**p < 0.01$, $***p < 0.001$, $****p < 0.0001$, ns: not significant.

Results

Single-cell transcriptomic atlas and cell typing in primary PDAC, lymphatic metastasis tumors, and hepatic metastatic tumors

To comprehensively understand the TME in PDAC with lymphatic metastasis, scRNA-seq was conducted on tissues from three LNN, three LNP PDAC patients, and one HM patient, all confirmed by histopathology (Fig. 1A, Supplementary Fig. 1, Supplementary Table 5). After quality control, a total of 32,504 cells from the cohort were included in the analysis. Annotation based on well-established markers classified these cells into 12 distinct cell types: MKI67$^+$ cells, acinar cells, ductal cells, T cells, B cells, plasma cells, macrophages/monocytes, neutrophils, mast cells, endothelial cells, endocrine cells, and fibroblasts (Supplementary Fig. 2A). To enhance the reliability of the data, scRNA-seq from our cohort was integrated with five publicly available datasets with intact clinical parameters (CRA001160, GSE197177, GSE229413, GSE242230/syn5241395, and OEP003254), expanding the analysis to a total of 161,184 cells from 61 patients (Fig. 1B–D, Supplementary Fig. 2B and C, Table 1, and Supplementary Table 6). All treatment-naive PDAC samples were surgically obtained from primary tumors, and all treatment-naive HM samples were surgically obtained from hepatic metastatic tissues. The UMAP plot revealed that the distribution of cell types varied across different groups (Fig. 1E, Supplementary Fig. 2D and E). Notably, myeloid cells exhibited significant heterogeneity between tissue types. Neutrophils were particularly more abundant in HM and LNP PDAC tissues compared with LNN PDAC tissues, whereas other immune cells showed minimal differences (Fig. 1F and G, Supplementary Fig. 2F and G). Although the DEGs in neutrophils were less abundant than in ductal or MKI67$^+$ cells, this indicates that, despite their lower numbers, neutrophils may play critical roles in lymphatic metastasis (Fig. 1H). These findings demonstrate

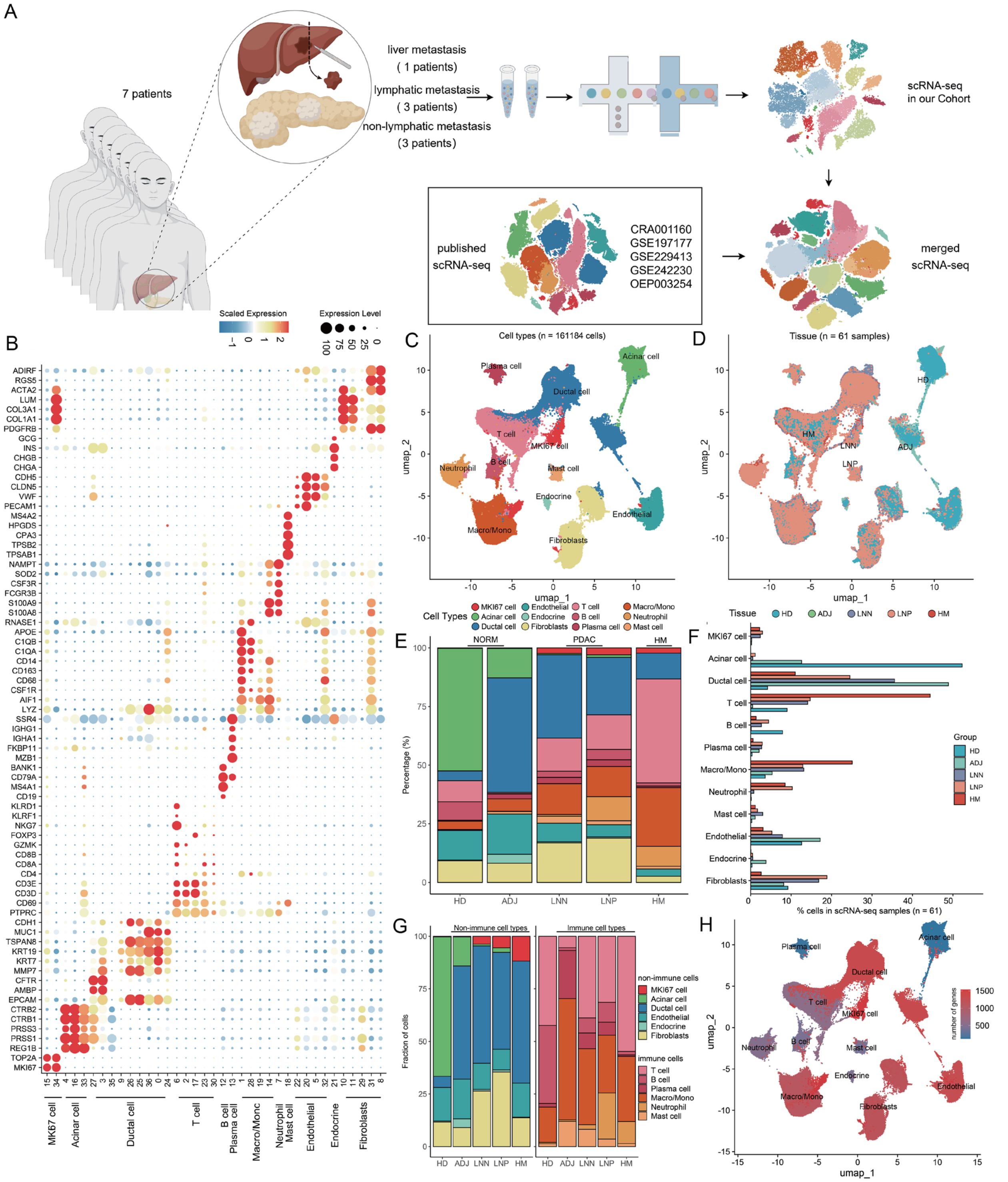

Fig. 1. Single-cell transcriptomic atlas and cell typing in primary PDAC and hepatic metastatic tumor. (A) Workflow of sample collection and data analysis in this study. (B) Dot plot showing representative marker genes across the 37 cell clusters. Dot size is proportional to the fraction of cells expressing specific genes. Color intensity corresponds to the relative expression of specific genes. (C) The UMAP plot displaying the merged scRNA-seq cell map, consisting of 37 cell clusters from 12 annotated cell types (n = 161,184 cells). The UMAP plot illustrates the distribution of all sequenced cells categorized by tissue origin. (D) The UMAP plot displaying the cell map in four tissue groups. (E) The bar plot showing the cell type abundance from different groups, including five HD, 12 ADJ, 15 LNN, 25 LNP, and four HM. (F) The bar plot displaying the cell type abundance in merged scRNA-seq, including 61 samples from six scRNA-seq datasets. (G) The bar plot showing the immune and non-immune cell type abundance in the integrated scRNA-seq. (H) The UMAP plot illustrating the distribution of major cell types and the number of DEGs in each cell type. NORM, normal pancreas; PDAC, pancreatic ductal adenocarcinoma; HD, healthy donor; ADJ, adjacent normal; LNN, lymph node-negative; LNP, lymph node-positive; HM, hepatic metastasis; UMAP, uniform manifold approximation and projection.

Table 1. Cell types and abundances in pancreatic ductal adenocarcinoma and hepatic metastases tissues detected by scRNA-seq

Cell types	NORM		PDAC		HM	Total Numbers of cells	Percentage (100%)
	HD	ADJ	LNN	LNP			
MKI67 cell	37	48	891	1,785	512	3,273	2.03
Acinar cell	10,067	2,631	202	687	1	13,588	8.43
Ductal cell	805	10,214	13,297	14,868	2,521	41,705	25.87
T cell	1,737	105	5,270	8,936	10,163	26,211	16.26
B cell	1,521	25	983	2,681	312	5,522	3.43
Plasma cell	71	441	1,010	1,745	139	3,406	2.11
Macro/Mono	686	1,110	4,915	7,814	5,749	20,274	12.58
Neutrophil	26	14	292	6,225	1,947	8,504	5.28
Mast cell	55	231	1,118	1,018	263	2,685	1.67
Endothelial	2,425	3,592	2,939	3,178	705	12,839	7.97
Endocrine	67	794	197	296	12	1,366	0.85
Fibroblast	1,772	1,709	6,287	11,450	593	21,811	13.53
Total	19,269	20,914	37,401	60,683	22,917	161,184	100

NORM, normal pancreas; PDAC, pancreatic ductal adenocarcinoma; LNN, lymph node-negative; LNP, lymph node-positive; HM, hepatic metastasis.

that neutrophils are the most differentially infiltrated cell type in PDAC and may play a central role in regulating LNM.

HM and LNP PDAC tissues show increased MDSC recruitment

To investigate whether MDSCs participate in regulating PDAC hepatic and lymphatic metastasis, the distribution of myeloid-derived cells in the cohort was analyzed alongside publicly available datasets. Seven distinct MDSC clusters were annotated based on DEGs and compared with other myeloid cell populations using the reported HLA-DR$^{-/dim}$ criteria (Fig. 2A). tSNE visualization showed the distribution of MDSCs across PDAC tissues and external datasets (Fig. 2B). In HM and LNP PDAC tissues, MDSCs were predominantly derived from monocytes/macrophages and neutrophils. These were categorized as monocytic MDSCs (M-MDSCs, marked by HLA-DR$^{-/dim}$CD11b$^+$CD33$^+$CD14$^+$CD66b$^-$) and PMN-MDSCs (marked by HLA-DR$^{-/dim}$CD11b$^+$CD33$^+$CD14$^-$CD66b$^+$), respectively. Both MDSC types exert immunosuppressive functions in the TME. Multiplex immunofluorescence staining further revealed the spatial distribution of these subsets, showing that PMN-MDSC infiltration positively correlated with lymphatic metastasis, whereas M-MDSCs did not demonstrate a similar association (Fig. 2C). Flow cytometry analysis confirmed an increased presence of MDSCs and PMN-MDSCs in LNP PDAC tissues, while M-MDSCs and early-stage MDSCs showed no difference between LNN and LNP tissues (Fig. 2D and Supplementary Fig. 3). Single-cell sequencing revealed that neutrophil-derived *CXCR2*$^+$, *IFIT2*$^+$, *IL1RN*$^+$, and *CXCR4*$^+$ MDSCs were significantly elevated in HM and LNP PDAC tissues compared with monocyte-derived MDSCs (Fig. 2E), suggesting that these neutrophil-derived subtypes may play a primary role in liver and lymphatic metastasis. The Gene Ontology analysis of the four neutrophil-derived MDSC clusters indicated that only *IL1RN*$^+$ and *CXCR2*$^+$ MDSCs were involved in immune suppression and leukocyte regulation (Fig. 2F). *CXCR2*$^+$ MDSCs were excluded from further analysis due to extensive prior studies. These findings highlight that MDSCs, particularly neutrophil-derived PMN-MDSCs, are increasingly recruited in HM and LNP PDAC tissues. Among them, *IL1RN*$^+$ MDSCs may represent the main immunosuppressive subtype contributing to hepatic and lymphatic metastasis.

IL1RN$^+$ MDSCs are increased in HM and LNP PDAC and correlate with worse survival outcomes

Given the potential immunosuppressive role of *IL1RN*$^+$ MDSCs, we examined whether these cells were elevated in HM and LNP PDAC and associated with poor prognosis. tSNE visualization confirmed the presence of *IL1RN*$^+$ MDSCs across all scRNA-seq datasets (Fig. 3A). The top five DEGs of *IL1RN*$^+$ MDSCs were displayed to highlight their molecular distinctions (Fig. 3B). IL1RA, encoded by *IL1RN*, was employed to stain for PMN-MDSCs (HLA-DR$^{-/dim}$CD11b$^+$CD33$^+$CD14$^-$CD66b$^+$IL1RA$^+$) and analyzed by flow cytometry and immunofluorescence staining in LNP PDAC tissues (Fig. 3C–E). Monocle2 was used to examine the developmental trajectory of *IL1RN*$^+$ MDSCs in the TME, revealing that CXCR4$^+$ MDSCs were at the trajectory's initiation point, while *IL1RN*$^+$ MDSCs were at the terminal stage (Fig. 3F). Along this trajectory, genes associated with immune suppression and dysfunction were upregulated, indicating progressive immunosuppression in HM and LNP PDAC (Fig. 3G). Among 16 PDAC patients, high and low IL1RA MDSC groups (n = 8 per group) were defined using a median cut-off of 2.46% of all CD45$^+$ cells, as determined by flow cytometry. Pathological parameters, including age, gender, differentiation, peripancreatic lymph node involvement, and neural invasion, were analyzed (Supplementary Table 7). IL1RA$^+$ MDSCs were correlated only with tumor size and peripancreatic lymph node invasion. Kaplan-Meier survival analysis indicated that higher IL1RA$^+$ MDSC proportions were associated with poorer prognosis (Fig. 3H). Overall, these findings suggest that *IL1RN*$^+$ MDSCs are elevated in HM and LNP PDAC and are linked to adverse survival outcomes.

IL1RN$^+$ MDSCs contribute to the establishment of an immunosuppressive microenvironment in PDAC

Given the increased presence of *IL1RN*$^+$ MDSCs in the LNP PDAC microenvironment, it was hypothesized that these cells may suppress antitumor immune responses by inter-

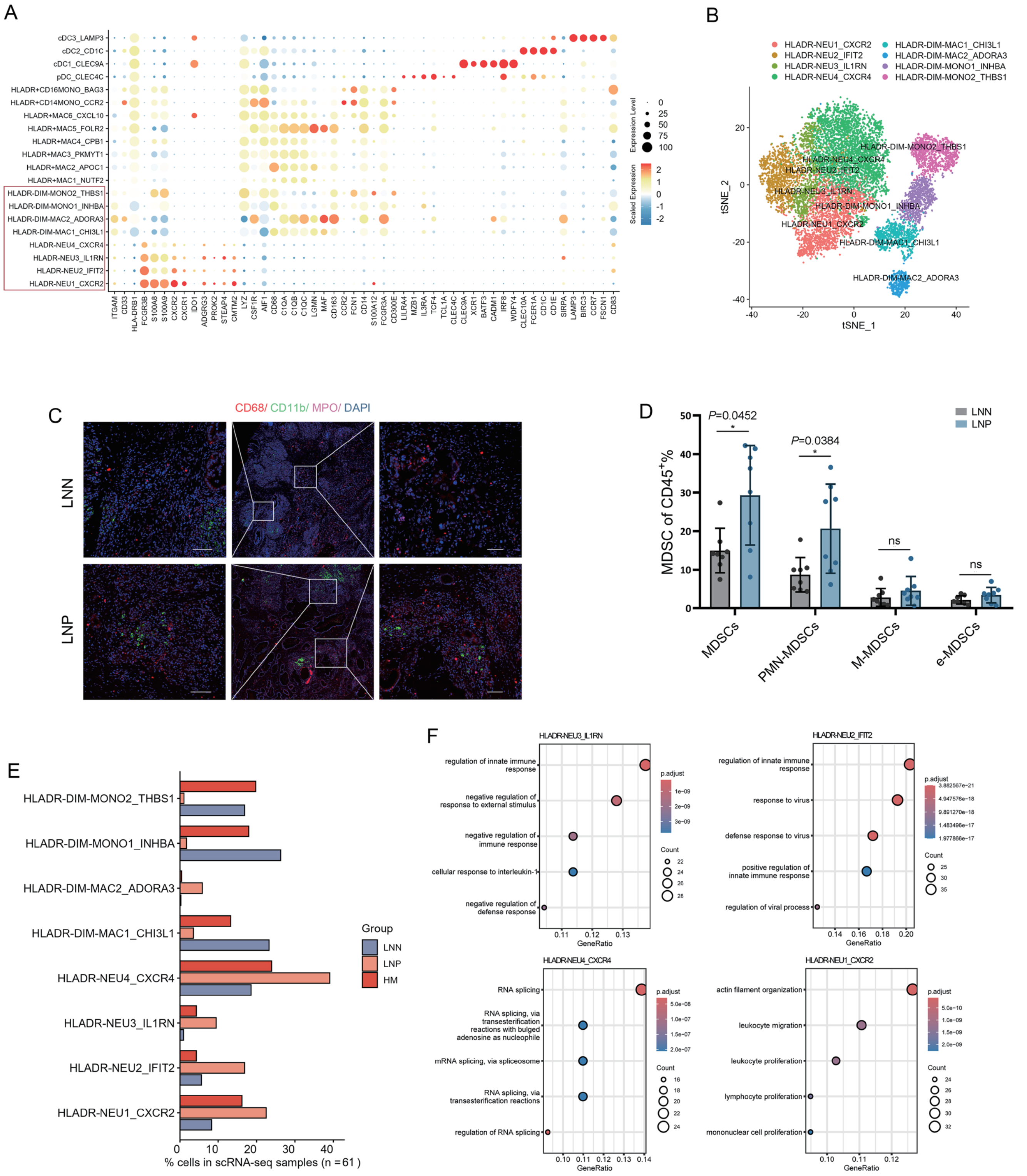

Fig. 2. Lymph node-positive PDAC tissues show increased MDSC recruitment. (A) Dot plot showing representative marker genes across myeloid cell clusters. Dot size is proportional to the fraction of cells expressing these genes. Color intensity corresponds to the relative expression of specific genes. (B) tSNE plot showing major MDSC subtypes identified by single-cell RNA sequencing of PDAC tissues from integrated scRNA-seq. (C) Representative images of staining using antibodies against MDSC markers. Scale bar = 100 µm. (D) Flow cytometry analysis of MDSCs obtained from 16 PDAC tissues, including eight LNN and eight LNP. (E) Bar plot showing MDSC abundance in samples from LNN, LNP, and HM groups. (F) GO_BP analysis of enriched processes in four subtypes of neutrophil-derived MDSCs. Data are presented as mean ± SD in (D). Statistical differences were assessed using a two-tailed Student's *t*-test. *$p < 0.05$. LNN, lymph node-negative; LNP, lymph node-positive; HM, hepatic metastasis; PDAC, pancreatic ductal adenocarcinoma; MDSCs, myeloid-derived suppressor cells.

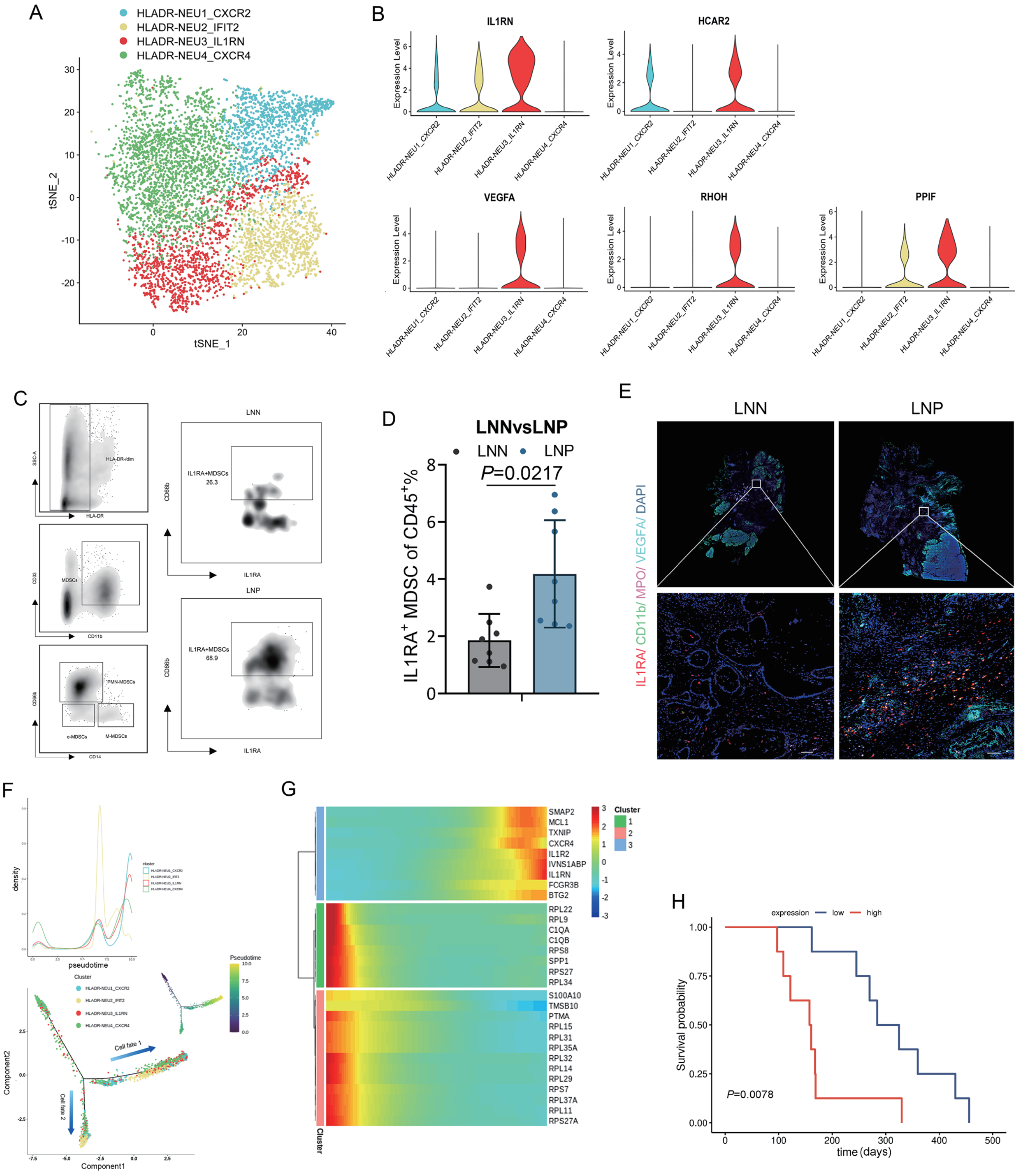

Fig. 3. IL1RA$^+$ MDSCs increase in LNP PDAC and correlate with worse survival outcomes. (A) tSNE plot showing the four neutrophil-derived MDSC subtypes. (B) The top five expressed genes of *IL1RN*$^+$ MDSCs in the four neutrophil-derived MDSC subsets. (C, D) Representative flow cytometry data and quantification graphs showing the proportion of IL1RA$^+$ MDSCs in LNN and LNP PDAC tissues. (E) Representative images of immunofluorescence staining of IL1RA$^+$ MDSCs in LNN and LNP PDAC tissues. Scale bar = 100 μm. (F) Trajectory of neutrophil-derived MDSCs along pseudotime in two-dimensional space. (G) Heatmap showing dynamic changes in gene expression along pseudotime. (H) Prognostic analysis of PDAC patients with low or high IL1RA$^+$ MDSC recruitment (stratified by the median IL1RA$^+$ MDSC proportion in all samples). Kaplan–Meier survival plots of 16 patients are shown. Data are presented as mean ± SD in (D). Statistical differences were assessed using a two-tailed Student's *t*-test. LNN, lymph node-negative; LNP, lymph node-positive; PDAC, pancreatic ductal adenocarcinoma; MDSCs, myeloid-derived suppressor cells.

acting with other immune cell types. To test this hypothesis, cell–cell interaction analysis was performed to visualize intercellular interactions. *IL1RN*$^+$ MDSCs were found to interact with multiple immune cell types in both LNN and LNP PDAC tissues (Fig. 4A). To further investigate the functional role of *IL1RN*$^+$ MDSCs, these cells were sorted for coculture experiments. Due to the intracellular localization of IL1RA, the sorting strategy was adjusted to isolate cells expressing the membrane protein HCAR2$^+$ and CXCR2$^{-/\mathrm{dim}}$ as a surrogate for *IL1RN*$^+$ MDSCs (Fig. 4B, Supplementary Fig. 4A). qRT-PCR confirmed that the sorted cells highly expressed *IL1RN* (Supplementary Fig. 4B). NK cells and T cells were isolated from human peripheral blood via flow cytometry and cocultured with CM from *IL1RN*$^+$ MDSCs for 48 h (Supplementary Fig. 4C). The results revealed that *IL1RN*$^+$ MDSCs directly inhibited NK cell effector functions via the IL-1β pathway. This inhibition was evidenced by a significant reduction in the mRNA expression levels of IFN-γ, LAMP1, and NCR3 (qRT-PCR), diminished lysosomal activity in target cells (LDH assay), and decreased secretion of IFN-γ, TNF-ɑ, and granzyme B (ELISA). Notably, this suppression was reversible upon IL-1β stimulation, which restored NK cell activation markers above baseline levels. In transwell experiments, NK cell cytotoxic functions were inhibited even without direct coculture with *IL1RN*$^+$ MDSCs, indicating that cell-cell contact was not required for this effect. Furthermore, IL-1 receptor blockade (raleukin, 50 ng/mL, MedChemExpress, Monmouth Junction, NJ, USA) in *IL1RN*$^{\mathrm{low}}$ MDSCs enhanced immunosuppressive activity, highlighting the pivotal role of IL-1 signaling in MDSC-mediated regulation of NK cells (Fig. 4B–D). Collectively, these results demonstrate that *IL1RN*$^+$ MDSCs inhibit NK cell cytotoxic functions via IL-1 secretion rather than direct contact. For T cell functions, qRT-PCR and ELISA assays were performed to measure IL-2 and IFN-γ (T cell activation) and IL-10 and TGF-β (T cell exhaustion) in cell lysates and supernatants, respectively (Fig. 4E and F). These assays revealed that *IL1RN*$^{\mathrm{high}}$ MDSCs inhibited T cell activation and promoted exhaustion through the IL-1 pathway compared with *IL1RN*$^{\mathrm{low}}$ MDSCs. For macrophage polarization, THP-1 cells were treated with PMA (100 ng/mL) for 48 h and subsequently exposed to CM from MDSCs. The mRNA and protein levels of IL-1β, TNF-ɑ, IL-10, and CCL13 were measured by qRT-PCR and ELISA, respectively (Fig. 4G and H). *IL1RN*$^{\mathrm{high}}$ MDSCs promoted polarization toward M2 macrophages while suppressing M1 polarization. IL-1β treatment inhibited the effect of *IL1RN*$^{\mathrm{high}}$ MDSCs, whereas IL-1 receptor inhibition promoted M2 polarization. Collectively, these data suggest that *IL1RN*$^+$ MDSCs contribute to remodeling an immunosuppressive microenvironment in PDAC via the IL-1 pathway.

IL1RN$^+$ *MDSCs promote PDAC progression in vitro and in vivo*

MDSCs are known not only to modulate immune cells in the TME but also to promote tumor progression by directly activating EMT and conferring stem-cell-like properties to tumor cells.[28,29] Therefore, the potential role of *IL1RN*$^+$ MDSCs in PDAC progression was investigated. Among the top five most highly expressed genes in *IL1RN*$^+$ MDSCs in LNP PDAC tissues, VEGFA was identified as a prominent molecule. Given its role in promoting lymphatic metastasis, the migration ability of PDAC cells was evaluated after coculture with *IL1RN*$^+$ MDSC-CM, with or without the VEGFR inhibitor axitinib (Fig. 5A). Transwell assays demonstrated that *IL1RN*$^+$ MDSCs enhanced PDAC cell migration, whereas axitinib reversed this effect (Fig. 5B). Western blotting and grayscale analysis quantified the expression of EMT markers (E-cadherin, N-cadherin, Claudin, and ZO-1) in PANC-1 cells treated with *IL1RN*$^+$ MDSC-CM with or without axitinib. The results revealed that *IL1RN*$^+$ MDSC-CM promoted EMT in PDAC cells, an effect reversed by axitinib (Fig. 5C). These data indicate that *IL1RN*$^+$ MDSCs promote PDAC progression via a VEGFA-dependent pathway. Further analysis of *OCT4*, *SOX2*, *NANOG*, and *KLF4* mRNA revealed that *IL1RN*$^+$ MDSCs enhance stemness in PANC-1 cells (Fig. 5D). To investigate tumorigenic potential *in vivo*, PDX models from LNP patients were established. Xenograft mice were subcutaneously injected with *IL1RN*$^+$ MDSCs isolated from LNP PDAC tissues and treated with or without axitinib. Consistently, tumors in mice receiving *IL1RN*$^+$ MDSCs were significantly larger, with higher tumor weights and volumes compared with controls. Axitinib treatment reversed this tumorigenic effect (Fig. 5E–H), as confirmed by hematoxylin and eosin staining (Fig. 5I). Overall, these data indicate that *IL1RN*$^+$ MDSCs promote PDAC progression both *in vitro* and *in vivo*.

Discussion

Notably, HM and LNM pose a significant challenge in treating PDAC, as they occur frequently and are often associated with poorer prognosis.[3,30] It is well documented that HM and LNM in PDAC are closely linked to an immunosuppressive TME.[7,20] During metastasis, disseminated orthotopic PDAC cells migrate into blood vessels and establish lesions at distant sites, such as the liver and lymph nodes. However, only a small proportion of disseminated tumor cells can survive in these organs, as the immune system monitors aberrant cells.[31] Metastatic PDAC cells in the liver encounter a harsh and strange microenvironment, different from the optimal orthotopic pancreatic TME. Consequently, most metastatic cells remain dormant when repelled by local hepatic cells.[32] To survive, metastatic PDAC cells actively remodel the liver microenvironment to support their persistence.[8] Over the past few decades, advancements in immunotherapy, particularly strategies aimed at remodeling the immunosuppressive TME in metastatic lesions, have revolutionized cancer treatment.[33] However, for PDAC patients, the application of immunotherapy remains limited.[7] One key reason for the limited efficacy of immunotherapy in PDAC is the incomplete characterization of immunosuppressive cell subtypes within the TME.

MDSCs, as a dominant cell population in tumor stroma, have emerged as a potential target for PDAC immunotherapy. These cells traffic into the PDAC microenvironment, where they suppress immune responses and inhibit the infiltration of cytotoxic immune cells.[34,35] Interestingly, although the TME of PDAC HM lesions and hepatocellular carcinoma (HCC) arises from different processes, TME remodeling in PDAC versus chronic fibrosis in HCC, the MDSCs present in both TMEs are relatively similar. For instance, both HCC and PDAC exhibit increased MDSC recruitment, which can serve as a prognostic biomarker.[36,37] MDSCs in both cancers create an immunosuppressive TME via the PD-L1 pathway.[14,38] Previous studies demonstrated that CXCR4-modified CAR-T cells could reduce the MDSC population and tumor volume in tumor-bearing mice by suppressing MDSC recruitment in PDAC.[39] However, the development of CXCR4-modified CAR-T cells is costly. Therefore, the present study focused on identifying novel therapeutic targets on MDSCs using existing drugs.

The increased recruitment of PMN-MDSCs in liver metastatic and LNP PDAC tissues was confirmed, correlating with HM and LNM in PDAC. Neutrophils have recently been identified as a primary source of PMN-MDSCs, contributing to the formation of an immunosuppressive TME that pro-

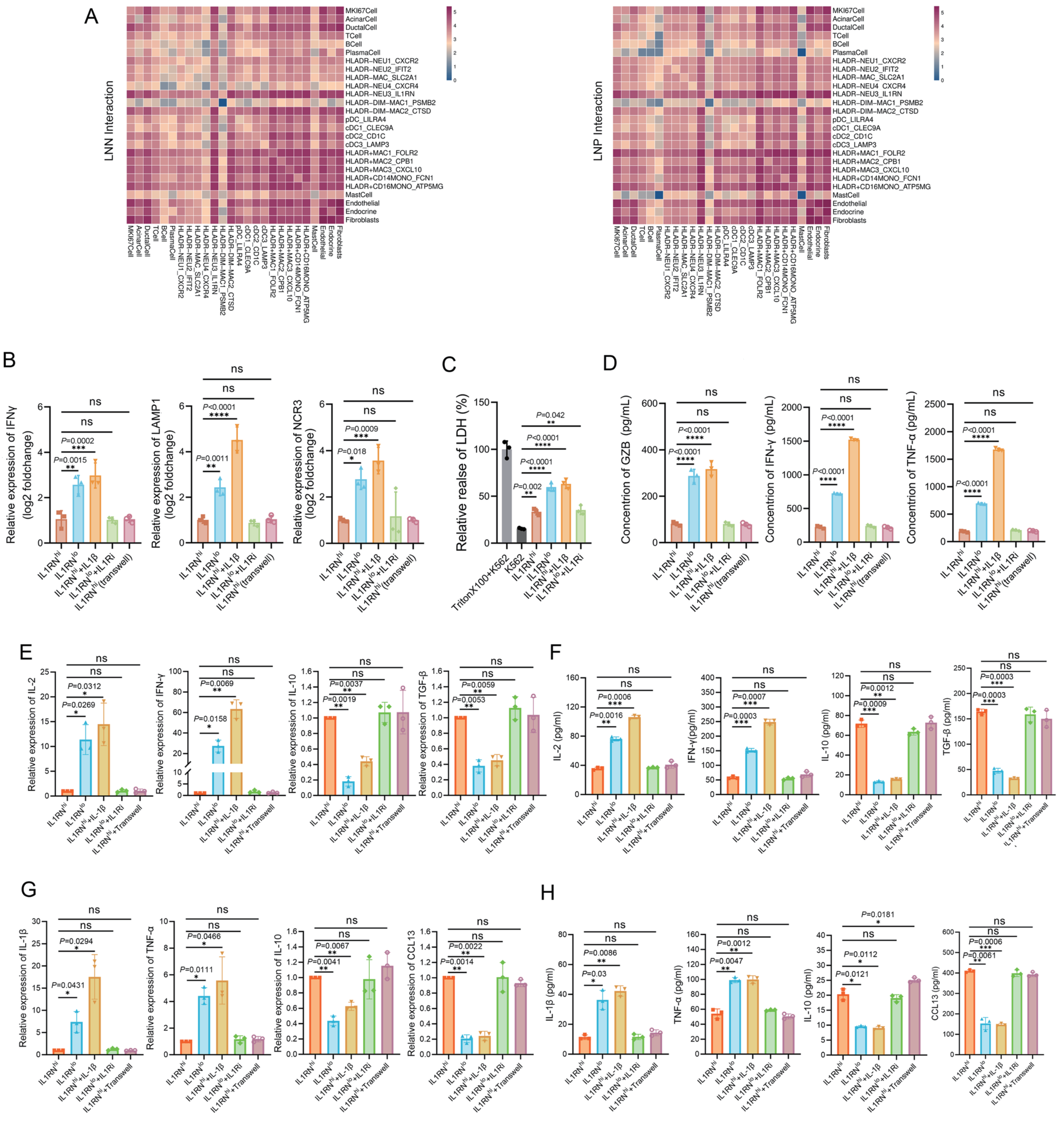

Fig. 4. *IL1RN*$^+$ MDSCs contribute to the establishment of an immunosuppressive microenvironment in PDAC. (A) Heatmap illustrating cell-cell interaction patterns in LNN and LNP samples. (B-D) *IL1RN*$^{\text{high}}$ MDSCs suppress NK cell activation and cytotoxicity: (B) Relative mRNA expression levels of IFN-γ, LAMP1, and NCR3 in NK cells under indicated co-cultures (fold change normalized to *IL1RN*$^{\text{high}}$ MDSC + NK co-culture group). (C) Cytotoxicity against K562 cells measured by LDH release (%; Triton X-100 + K562 = maximum lysis control (100%); K562 alone = baseline control). (D) Concentrations (pg/mL) of GZB, IL-1β, and TNF-α in co-culture supernatants (ELISA). (E, F) *IL1RN*$^{\text{high}}$ MDSCs inhibit macrophage polarization toward M2 phenotype via a non-contact mechanism: (E) Relative mRNA expression levels of IFN-γ, IL-2, IL-10, and TGF-β1 in macrophages under indicated co-cultures (fold change normalized to *IL1RN*$^{\text{high}}$ MDSC + macrophage co-culture). (F) Concentrations (pg/mL) of IFN-γ, IL-2, IL-10, and TGF-β in co-culture supernatants (ELISA). (G, H) *IL1RN*$^{\text{high}}$ MDSCs suppress T cell activation and proliferation via a non-contact mechanism: (G) Relative mRNA expression levels of IL-1β, CCL13, IL-10, and TNF-α in suppressor T cells under indicated co-cultures (fold change normalized to *IL-1RN*$^{\text{high}}$ MDSC + suppressor T cell co-culture). (H) Concentrations (pg/mL) of IL-1β, CCL13, IL-10, and TNF-α in co-culture supernatants (ELISA). Data are represented as mean ± SD of three independent biological replicates. Statistical significance was determined by one-way ANOVA with Dunnett's post-hoc test: $^{ns}p \geq 0.05$; $^*p < 0.05$; $^{**}p < 0.01$; $^{***}p < 0.001$; $^{****}p < 0.0001$. PDAC, pancreatic ductal adenocarcinoma; MDSCs, myeloid-derived suppressor cells; LNN, lymph node-negative; LNP, lymph node-positive; GZB, Granzyme B.

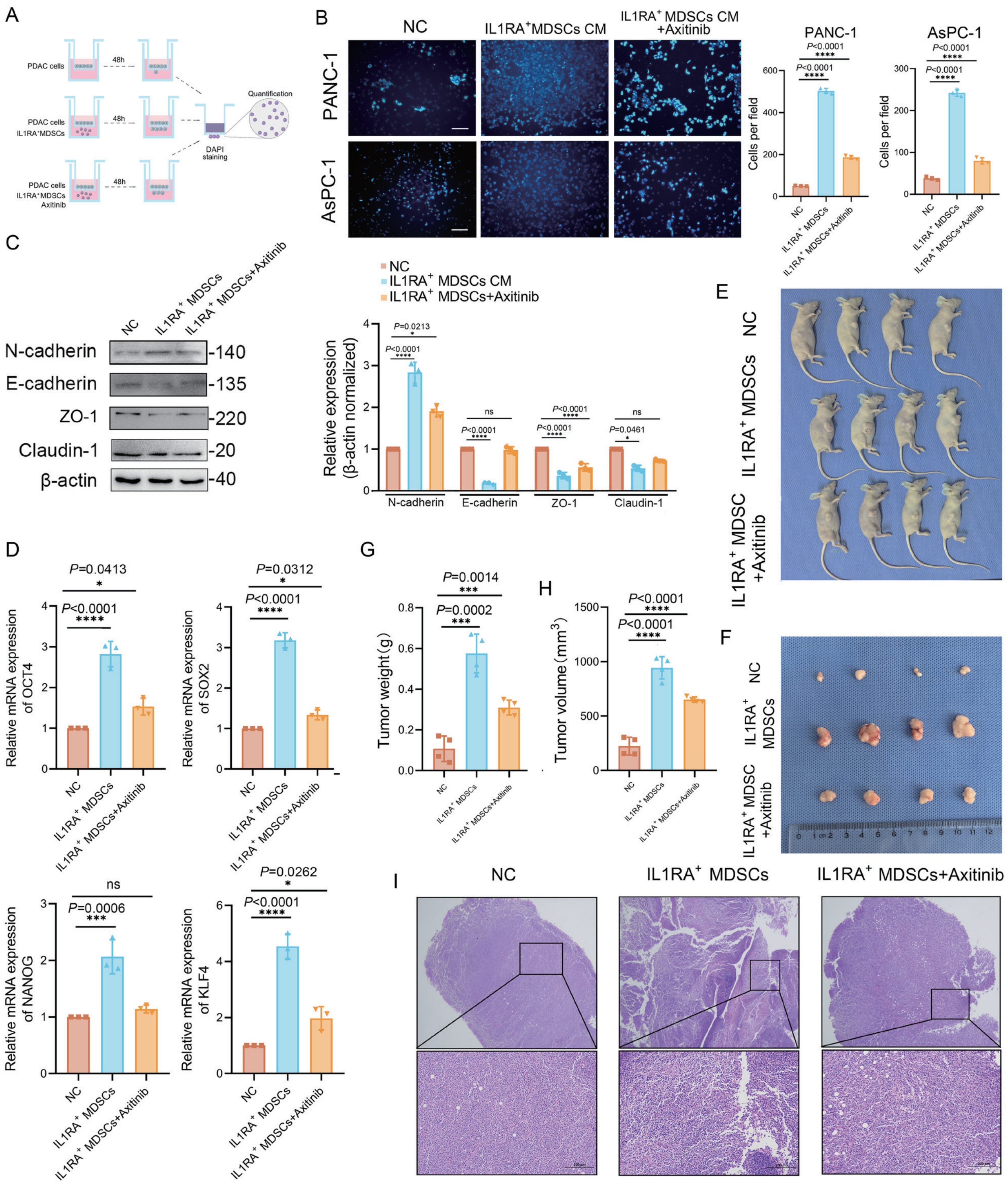

Fig. 5. *IL1RN*$^+$ MDSCs promote PDAC progression *in vitro* and *in vivo*. (A) Schematic illustration of *IL1RN*$^+$ MDSC–PDAC co-culture system. (B) Transwell migration assays in PANC-1 and ASPC-1 cells treated with normal medium (Control), IL1RA$^+$ MDSC-conditioned medium (IL1RA$^+$ MDSC CM), or IL1RA$^+$ MDSC CM + Axitinib. Scale bar = 50 µm. (C) Western blot analysis of EMT markers (N-cadherin, E-cadherin, ZO-1, Claudin-1) in PANC-1 cells under treatments identical to (B); β-actin was detected as a control. Grayscale was determined using ImageJ. (D) Relative expression of stemness-related mRNA after treatment with IL1RA$^+$ MDSC CM or IL1RA$^+$ MDSC CM + Axitinib. (E) Representative images of subcutaneous tumors in BALB/c nude mice from the PDX model: Group 1 (Control, tumor tissue only); Group 2 (tumor tissue co-implanted with *IL1RN*$^+$ MDSCs); Group 3 (tumor tissue co-implanted with *IL1RN*$^+$ MDSCs + Axitinib). (F) Excised tumor tissues from (E). (G, H) Tumor weights (G) and volumes (H) from the mouse model presented as bar graphs. (I) Representative H&E staining images of mouse pancreatic tumor tissues. Scale bar = 100 µm. Data are represented as mean ± SD of three independent biological replicates in (B) and four independent replicates in (F and G). Statistical significance was determined by one-way ANOVA with Dunnett's post-hoc test: $^{ns}p \geq 0.05$; $^*p < 0.05$; $^{***}p < 0.001$; $^{****}p < 0.0001$. PDAC, pancreatic ductal adenocarcinoma; MDSCs, myeloid-derived suppressor cells.

motes necrosis and metastasis in multiple tumor types.[27,40] For instance, CD11b$^+$ LY6G$^+$ Ly6C^{low} and STAT3-activated neutrophils can exert immunosuppressive functions as PMN-MDSCs.[41] In the present study, neutrophils were identified as one of the most differentially expressed cell types in both HM and LNP PDAC tissues. The increased neutrophil recruitment in these tissues demonstrates that specific neutrophil subtypes may function as PMN-MDSCs, facilitating metastasis.

Four distinct subtypes of neutrophil-derived MDSCs were identified in HM and LNP PDAC tissues: *CXCR2*$^+$, *IFIT2*$^+$, *IL1RN*$^+$, and *CXCR4*$^+$ MDSCs. Among them, *IL1RN*$^+$ MDSCs have not been well characterized but were identified as a significant population involved in immune suppression in the TME and as a predictor of prognosis. IL1RA$^+$ MDSCs were found to impair macrophage, NK cell, and T cell functions via the IL-1 pathway. IL1RA, encoded by *IL1RN*, is a member of the IL-1 cytokine family and serves as a competitive inhibitor of IL-1 ligands.[15] IL1RA plays a notable role in blocking the IL-1 pathway and preventing overactive immune responses. Previous studies reported that IL1RA promotes immunosuppression and tumor cell proliferation in prostate cancer and glioma, establishing it as a pro-tumorigenic cytokine in the TME.[17,18] However, the role of IL1RA in HM or LNM of PDAC has not been fully elucidated. Similarly, IL-1 is recognized as a pro-tumoral cytokine that accelerates tumor progression by recruiting myeloid cells to establish an immunosuppressive environment, promoting angiogenesis, activating endothelial cells, and skewing lymphoid cells.[42] Therefore, the function of the IL-1 pathway in the TME remains complex, as both IL-1 and IL1RA have been implicated in promoting tumor progression, while IL1RA directly inhibits the IL-1 pathway. These paradoxical findings complicate the use of IL-1-targeted immunotherapies in PDAC. Accordingly, the roles of IL1RA$^+$ MDSCs in HM and LNP PDAC tissues were further explored.

Although IL1-mediated chronic inflammation is a common driver of tumor progression, IL1 can also act as a licensing signal to activate T cells and NK cells in colon adenocarcinoma and neuroblastoma.[43,44] The results of the present study confirmed that IL1RA$^+$ MDSCs are increasingly recruited in HM and LNP PDAC TMEs and serve as a potent immunosuppressive population, inhibiting the cytotoxic functions of NK and T cells and promoting M2 macrophage polarization via suppression of the IL1 pathway. These findings highlight IL1RA$^+$ MDSC populations as potential prognostic biomarkers for HM and LNM. Moreover, a potent and short-term regimen targeting IL1RA$^+$ MDSCs could reactivate anti-tumor immune responses in PDAC.

VEGFA has been characterized as a dominant driver of angiogenesis in tumor progression, and targeting VEGFA has emerged as a promising therapeutic strategy in multiple cancers, including HCC.[45] Additionally, VEGFA has been validated to activate the EMT pathway, promoting lymphatic metastasis in esophageal squamous cell carcinoma, indicating that VEGFA-targeted therapy may be effective in PDAC.[46] However, clinical outcomes for PDAC patients receiving VEGFA-targeted therapies remain unsatisfactory.[47] This failure is largely attributed to the limited efficacy of VEGF inhibition alone. Consequently, strategies combining immunotherapy with targeted therapy have been investigated to enhance treatment efficacy in PDAC.[48]

Importantly, VEGFA was identified as one of the top five DEGs in IL1RA$^+$ MDSCs, presenting the potential to combine immunotherapy and targeted therapy by simultaneously inhibiting IL1RA$^+$ MDSCs. Axitinib, a well-known VEGFR inhibitor that blocks VEGFR1–3, was used to validate this approach. In HCC, the combination of axitinib and avelumab achieved a 31.8% objective response rate.[49] Moreover, VEGF antibodies have been shown to inhibit the EMT pathway in breast cancer and HCC.[50] Our results confirmed that VEGFR inhibition with axitinib reversed the migratory capacity and EMT changes induced by IL1RA$^+$ MDSCs in PDAC, providing further evidence that axitinib can suppress the EMT pathway through IL1RA$^+$ MDSCs. Since axitinib has been successfully applied in HCC, it may represent a promising treatment for PDAC with HM and LNM. Overall, these findings highlight the potential of combining immunotherapy and targeted therapy by inhibiting both IL1RA$^+$ MDSC-mediated IL1 signaling and EMT pathways.

Collectively, our findings reveal a novel IL1RA$^+$ MDSC subtype that promotes hepatic and LNM in PDAC, highlighting the prognostic and therapeutic potential of targeting these cells to remodel the immunosuppressive TME via IL1 pathway blockade and VEGF inhibition. However, the limited availability of liver metastasis tissues and the need for further investigation into EMT-related mechanisms remain constraints of this study, warranting more comprehensive validation in future research.

Conclusions

IL1RA$^+$ MDSCs have been identified as novel regulatory immune cells that are significantly enriched in the HM and LNP PDAC microenvironment and are associated with poor prognosis. This study confirmed that IL1RA$^+$ MDSCs express high levels of IL1RA and VEGFA and interact with NK cells, T cells, and macrophages to establish an immunosuppressive microenvironment via the IL1 pathway. Furthermore, IL1RA$^+$ MDSCs promote PDAC progression through the VEGF pathway in both *in vitro* and *in vivo* models. These findings highlight the potential of targeting IL1RA$^+$ MDSCs in the TME as a promising therapeutic strategy for PDAC.

Acknowledgments

We would like to thank the First Hospital of Jilin University and the Flow Cytometry Platform in the Core Facility of the First Hospital of Jilin University. We also appreciate the funding from the National Natural Science Foundation of China and the National Natural Science Foundation of Jilin Province.

Funding

This work was supported by the National Natural Science Foundation of China under Grant [No. 82473314, 82273276, 81970529] and the National Natural Science Foundation of Jilin Province under Grant [20200201546JC].

Conflict of interest

The authors have no conflict of interests related to this publication.

Author contributions

Experiment conception and design (FW, HaiL , JZ), drafting of the manuscript (HuanL, JZ), Figure preparation (HuanL, SL, XP, HanL, JZ), clinical specimen preparation, flow cytometry (HuanL, HanL). All authors read and approved the submitted version of the manuscript.

Ethical statement

The acquisition of patient tissues was approved by the Medical Ethics Committee of the First Affiliated Hospital of Jilin University (Approval No. 2019180), in accordance with the Helsinki Declaration as revised in 2024. All patients provided written informed consent. All animal experiments were conducted in accordance with the regulations of the Institutional Animal Care and Use Committee of Changchun Veterinary Research Institute (Approval No. 2024-11-066). All animals revived human care.

Data sharing statement

The raw scRNA-seq data (FASTQ files) generated in this study, including six PDAC samples and one hepatic metastasis sample, have been deposited in SRA under the accession numbers SAMN47538140–42, SAMN5021233–35, and SAMN5021237. The publicly available scRNA-seq datasets used in this study can be accessed as follows: The Genome Sequence Archive under project PRJCRA001160, which includes 11 adjacent normal pancreas samples and 24 PDAC samples. The GSE197177 dataset, which includes three hepatic metastasis samples and one adjacent normal pancreas sample, was retrieved from the Gene Expression Omnibus database. The GSE229413 dataset, which includes five healthy donor pancreas samples, was retrieved from the Gene Expression Omnibus database. The GSE242230/syn5241395 dataset, which includes five PDAC samples, is available for download via dbGaP from the Human Tumor Atlas Network data portal (https://humantumoratlas.org). The OEP003254 dataset, retrieved from the National Omics Data Encyclopedia with accession code OEP003254, includes five PDAC samples.

References

[1] Stoop TF, Javed AA, Oba A, Koerkamp BG, Seufferlein T, Wilmink JW, *et al*. Pancreatic cancer. Lancet 2025;405(10485):1182–1202. doi:10.1016/S0140-6736(25)00261-2, PMID:40187844.

[2] Huang L, Jansen L, Balavarca Y, Molina-Montes E, Babaei M, van der Geest L, *et al*. Resection of pancreatic cancer in Europe and USA: an international large-scale study highlighting large variations. Gut 2019;68(1):130–139. doi:10.1136/gutjnl-2017-314828, PMID:29158237.

[3] Luo Y, Li Z, Kong Y, He W, Zheng H, An M, *et al*. KRAS mutant-driven SUMOylation controls extracellular vesicle transmission to trigger lymphangiogenesis in pancreatic cancer. J Clin Invest 2022;132(14):e157644. doi:10.1172/JCI157644, PMID:35579947.

[4] Zheng B, Qu J, Ohuchida K, Feng H, Chong SJF, Yan Z, *et al*. LAMA4 upregulation is associated with high liver metastasis potential and poor survival outcome of Pancreatic Cancer. Theranostics 2020;10(22):10274–10289. doi:10.7150/thno.47001, PMID:32929348.

[5] Kong Y, Li Y, Luo Y, Zhu J, Zheng H, Gao B, *et al*. circNFIB1 inhibits lymphangiogenesis and lymphatic metastasis via the miR-486-5p/PIK3R1/VEGF-C axis in pancreatic cancer. Mol Cancer 2020;19(1):82. doi:10.1186/s12943-020-01205-6, PMID:32366257.

[6] Karaman S, Detmar M. Mechanisms of lymphatic metastasis. J Clin Invest 2014;124(3):922–928. doi:10.1172/JCI71606, PMID:24590277.

[7] Farhangnia P, Khorramdelazad H, Nickho H, Delbandi AA. Current and future immunotherapeutic approaches in pancreatic cancer treatment. J Hematol Oncol 2024;17(1):40. doi:10.1186/s13045-024-01561-6, PMID:38835055.

[8] Xie Z, Gao Y, Ho C, Li L, Jin C, Wang X, *et al*. Exosome-delivered CD44v6/C1QBP complex drives pancreatic cancer liver metastasis by promoting fibrotic liver microenvironment. Gut 2022;71(3):568–579. doi:10.1136/gutjnl-2020-323014, PMID:33827783.

[9] Alewine C. Macrophages Under the Influence of Tumor Mesothelin Weaken Host Defenses against Pancreatic Cancer Metastasis. Cancer Res 2024;84(4):513–514. doi:10.1158/0008-5472.CAN-23-4036, PMID:38356442.

[10] Irshad S, Flores-Borja F, Lawler K, Monypenny J, Evans R, Male V, *et al*. RORγt(+) Innate Lymphoid Cells Promote Lymph Node Metastasis of Breast Cancers. Cancer Res 2017;77(5):1083–1096. doi:10.1158/0008-5472.CAN-16-0598, PMID:28082403.

[11] Uzunparmak B, Sahin IH. Pancreatic cancer microenvironment: a current dilemma. Clin Transl Med 2019;8(1):2. doi:10.1186/s40169-019-0221-1, PMID:30645701.

[12] Lasser SA, Ozbay Kurt FG, Arkhypov I, Utikal J, Umansky V. Myeloid-derived suppressor cells in cancer and cancer therapy. Nat Rev Clin Oncol 2024;21(2):147–164. doi:10.1038/s41571-023-00846-y, PMID:38191922.

[13] Tcyganov EN, Hanabuchi S, Hashimoto A, Campbell D, Kar G, Slidel TW, *et al*. Distinct mechanisms govern populations of myeloid-derived suppressor cells in chronic viral infection and cancer. J Clin Invest 2021;131(16):e145971. doi:10.1172/JCI145971, PMID:34228641.

[14] Lu C, Liu Z, Klement JD, Yang D, Merting AD, Poschel D, *et al*. WDR5-H3K4me3 epigenetic axis regulates OPN expression to compensate PD-L1 function to promote pancreatic cancer immune escape. J Immunother Cancer 2021;9(7):e002624. doi:10.1136/jitc-2021-002624, PMID:34326167.

[15] Mantovani A, Dinarello CA, Molgora M, Garlanda C. Interleukin-1 and Related Cytokines in the Regulation of Inflammation and Immunity. Immunity 2019;50(4):778–795. doi:10.1016/j.immuni.2019.03.012, PMID:30995499.

[16] Fang Z, Jiang J, Zheng X. Interleukin-1 receptor antagonist: An alternative therapy for cancer treatment. Life Sci 2023;335:122276. doi:10.1016/j.lfs.2023.122276, PMID:37977354.

[17] Liu YN, Liu MK, Wen YC, Li CH, Yeh HL, Dung PVT, *et al*. Binding of interleukin-1 receptor antagonist to cholinergic receptor muscarinic 4 promotes immunosuppression and neuroendocrine differentiation in prostate cancer. Cancer Lett 2024;598:217090. doi:10.1016/j.canlet.2024.217090, PMID:38945201.

[18] Wang K, Liu H, Liu J, Wang X, Teng L, Zhang J, *et al*. IL1RN mediates the suppressive effect of methionine deprivation on glioma proliferation. Cancer Lett 2019;454:146–157. doi:10.1016/j.canlet.2019.04.004, PMID:30978442.

[19] Huang Y, Hong W, Wei X. The molecular mechanisms and therapeutic strategies of EMT in tumor progression and metastasis. J Hematol Oncol 2022;15(1):129. doi:10.1186/s13045-022-01347-8, PMID:36076302.

[20] Liu M, Zhang Y, Yang J, Zhan H, Zhou Z, Jiang Y, *et al*. Zinc-Dependent Regulation of ZEB1 and YAP1 Coactivation Promotes Epithelial-Mesenchymal Transition Plasticity and Metastasis in Pancreatic Cancer. Gastroenterology 2021;160(5):1771–1783.e1. doi:10.1053/j.gastro.2020.12.077, PMID:33421513.

[21] Ghantous Y, Mozalbat S, Nashef A, Abdol-Elraziq M, Sudri S, Araidy S, *et al*. EMT Dynamics in Lymph Node Metastasis of Oral Squamous Cell Carcinoma. Cancers (Basel) 2024;16(6):1185. doi:10.3390/cancers16061185, PMID:38539520.

[22] Li Z, Yu CP, Zhong Y, Liu TJ, Huang QD, Zhao XH, *et al*. Sam68 expression and cytoplasmic localization is correlated with lymph node metastasis as well as prognosis in patients with early-stage cervical cancer. Ann Oncol 2012;23(3):638–646. doi:10.1093/annonc/mdr290, PMID:21700735.

[23] Farahzadi R, Valipour B, Fathi E, Pirmoradi S, Molavi O, Montazersaheb S, *et al*. Oxidative stress regulation and related metabolic pathways in epithelial-mesenchymal transition of breast cancer stem cells. Stem Cell Res Ther 2023;14(1):342. doi:10.1186/s13287-023-03571-6, PMID:38017510.

[24] Mendoza-Rodríguez M, Arévalo Romero H, Fuentes-Pananá EM, Ayala-Sumuano JT, Meza I. IL-1β induces up-regulation of BIRC3, a gene involved in chemoresistance to doxorubicin in breast cancer cells. Cancer Lett 2017;390:39–44. doi:10.1016/j.canlet.2017.01.005, PMID:28093282.

[25] Chockley PJ, Chen J, Chen G, Beer DG, Standiford TJ, Keshamouni VG. Epithelial-mesenchymal transition leads to NK cell-mediated metastasis-specific immunosurveillance in lung cancer. J Clin Invest 2018;128(4):1384–1396. doi:10.1172/JCI97611, PMID:29324443.

[26] Zhang J, Lv S, Peng X, Liu H, Guo J, Liu Z, *et al*. CircERC1 facilitates chemoresistance through inhibiting pyroptosis and remodeling extracellular matrix in pancreatic cancer. Mol Cancer 2025;24(1):185. doi:10.1186/s12943-025-02385-9, PMID:40605033.

[27] Jackson C, Cherry C, Bom S, Dykema AG, Wang R, Thompson E, *et al*. Distinct myeloid-derived suppressor cell populations in human glioblastoma. Science 2025;387(6731):eabm5214. doi:10.1126/science.abm5214, PMID:39818911.

[28] He S, Zheng L, Qi C. Myeloid-derived suppressor cells (MDSCs) in the tumor microenvironment and their targeting in cancer therapy. Mol Cancer 2025;24(1):5. doi:10.1186/s12943-024-02208-3, PMID:39780248.

[29] Peng D, Tanikawa T, Li W, Zhao L, Vatan L, Szeliga W, *et al*. Myeloid-Derived Suppressor Cells Endow Stem-like Qualities to Breast Cancer Cells through IL6/STAT3 and NO/NOTCH Cross-talk Signaling. Cancer Res 2016;76(11):3156–3165. doi:10.1158/0008-5472.CAN-15-2528, PMID:27197152.

[30] Wang X, Luo G, Zhang K, Cao J, Huang C, Jiang T, *et al*. Hypoxic Tumor-Derived Exosomal miR-301a Mediates M2 Macrophage Polarization via PTEN/PI3Kγ to Promote Pancreatic Cancer Metastasis. Cancer Res 2018;78(16):4586–4598. doi:10.1158/0008-5472.CAN-17-3841, PMID:29880482.

[31] Wculek SK, Malanchi I. Neutrophils support lung colonization of metastasis-initiating breast cancer cells. Nature 2015;528(7582):413–417. doi:10.1038/nature16140, PMID:26649828.

[32] Albrengues J, Shields MA, Ng D, Park CG, Ambrico A, Poindexter ME, *et al*. Neutrophil extracellular traps produced during inflammation awaken dormant cancer cells in mice. Science 2018;361(6409):eaao4227. doi:10.1126/science.aao4227, PMID:30262472.

[33] Yang K, Halima A, Chan TA. Antigen presentation in cancer - mechanisms and clinical implications for immunotherapy. Nat Rev Clin Oncol 2023;20(9):604–623. doi:10.1038/s41571-023-00789-4, PMID:37328642.

[34] Liu X, Tang R, Xu J, Tan Z, Liang C, Meng Q, *et al*. CRIP1 fosters MDSC trafficking and resets tumour microenvironment via facilitating NF-κB/p65 nuclear translocation in pancreatic ductal adenocarcinoma. Gut 2023;72(12):2329–2343. doi:10.1136/gutjnl-2022-329349, PMID:37541772.

[35] Tong X, Xiao M, Yang J, Xu J, Wang W, Yu X, *et al*. The TMBIM1-YBX1 axis orchestrates MDSC recruitment and immunosuppressive microenvironment in pancreatic cancer. Theranostics 2025;15(7):2794–2813. doi:10.7150/thno.111180, PMID:40083936.

[36] Yu SJ, Ma C, Heinrich B, Brown ZJ, Sandhu M, Zhang Q, *et al*. Targeting the crosstalk between cytokine-induced killer cells and myeloid-derived suppressor cells in hepatocellular carcinoma. J Hepatol 2019;70(3):449–457. doi:10.1016/j.jhep.2018.10.040, PMID:30414862.

[37] Zhang J, Xu X, Shi M, Chen Y, Yu D, Zhao C, *et al*. CD13(hi) Neutrophil-like myeloid-derived suppressor cells exert immune suppression through Arginase 1 expression in pancreatic ductal adenocarcinoma. Oncoimmunology 2017;6(2):e1258504. doi:10.1080/2162402X.2016.1258504, PMID:28344866.

[38] Xie M, Lin Z, Ji X, Luo X, Zhang Z, Sun M, *et al*. FGF19/FGFR4-mediated elevation of ETV4 facilitates hepatocellular carcinoma metastasis by upregulating PD-L1 and CCL2. J Hepatol 2023;79(1):109–125. doi:10.1016/j.jhep.2023.02.036, PMID:36907560.

[39] Sun R, Sun Y, Wu C, Liu Y, Zhou M, Dong Y, *et al*. CXCR4-modified CAR-T cells suppresses MDSCs recruitment via STAT3/NF-κB/SDF-1α axis to enhance efficacy against pancreatic cancer. Mol Ther 2023;31(11):3193–3209. doi:10.1016/j.ymthe.2023.09.010, PMID:37735875.

[40] Adrover JM, Han X, Sun L, Fujii T, Sivetz N, Daßler-Plenker J, *et al*. Neutrophils drive vascular occlusion, tumour necrosis and metastasis. Nature 2025;645(8080):484–495. doi:10.1038/s41586-025-09278-3, PMID:40670787.

[41] Chalmin F, Ladoire S, Mignot G, Vincent J, Bruchard M, Remy-Martin JP, *et al*. Membrane-associated Hsp72 from tumor-derived exosomes mediates STAT3-dependent immunosuppressive function of mouse and human myeloid-derived suppressor cells. J Clin Invest 2010;120(2):457–471. doi:10.1172/JCI40483, PMID:20093776.

[42] Garlanda C, Mantovani A. Interleukin-1 in tumor progression, therapy, and prevention. Cancer Cell 2021;39(8):1023–1027. doi:10.1016/j.ccell.2021.04.011, PMID:33989512.

[43] Jain A, Song R, Wakeland EK, Pasare C. T cell-intrinsic IL-1R signaling licenses effector cytokine production by memory CD4 T cells. Nat Commun 2018;9(1):3185. doi:10.1038/s41467-018-05489-7, PMID:30093707.

[44] Landolina N, Mariotti FR, Pelosi A, D'Oria V, Ingegnere T, Alicata C, *et al*. The anti-inflammatory cytokine IL-37 improves the NK cell-mediated antitumor response. Oncoimmunology 2024;13(1):2297504. doi:10.1080/2162402X.2023.2297504, PMID:38170019.

[45] Li S, Li K, Wang K, Yu H, Wang X, Shi M, *et al*. Low-dose radiotherapy combined with dual PD-L1 and VEGFA blockade elicits antitumor response in hepatocellular carcinoma mediated by activated intratumoral CD8(+) exhausted-like T cells. Nat Commun 2023;14(1):7709. doi:10.1038/s41467-023-43462-1, PMID:38001101.

[46] Li Y, Ladd Z, Xiong Z, Bui-Linh C, Paiboonrungruang C, Subramaniyan B, *et al*. Lymphatic Metastasis of Esophageal Squamous Cell Carcinoma: The Role of NRF2 and Therapeutic Strategies. Cancers (Basel) 2025;17(11):1853. doi:10.3390/cancers17111853, PMID:40507333.

[47] Li S, Xu HX, Wu CT, Wang WQ, Jin W, Gao HL, *et al*. Angiogenesis in pancreatic cancer: current research status and clinical implications. Angiogenesis 2019;22(1):15–36. doi:10.1007/s10456-018-9645-2, PMID:30168025.

[48] Liu L, Huang X, Shi F, Song J, Guo C, Yang J, *et al*. Combination therapy for pancreatic cancer: anti-PD-(L)1-based strategy. J Exp Clin Cancer Res 2022;41(1):56. doi:10.1186/s13046-022-02273-w, PMID:35139879.

[49] Kudo M, Motomura K, Wada Y, Inaba Y, Sakamoto Y, Kurosaki M, *et al*. Avelumab in Combination with Axitinib as First-Line Treatment in Patients with Advanced Hepatocellular Carcinoma: Results from the Phase 1b VEGF Liver 100 Trial. Liver Cancer 2021;10(3):249–259. doi:10.1159/000514420, PMID:34239811.

[50] Niu M, Yi M, Wu Y, Lyu L, He Q, Yang R, *et al*. Synergistic efficacy of simultaneous anti-TGF-β/VEGF bispecific antibody and PD-1 blockade in cancer therapy. J Hematol Oncol 2023;16(1):94. doi:10.1186/s13045-023-01487-5, PMID:37573354.